J. Appl. Comput. Mech., 8(4) (2022) 1163-1175
DOI: 10.22055/JACM.2021.38204.3177

ISSN: 2383-4536
jacm.scu.ac.ir

Shahid Chamran University of Ahvaz

Journal of Applied and Computational Mechanics

Research Paper

Magnetized Bi-convective Nanofluid Flow and Entropy Production Using Temperature-sensitive Base Fluid Properties: A Unique Approach

Tapas Barman[1], S. Roy[1], Ali J. Chamkha[2]

[1] Mathematics, IIT Madras, India, Email: sjroy@iitm.ac.in

[2] Faculty of Engineering, Kuwait College of Science and Technology, Doha, Kuwait, Email: a.chamkha@kcst.edu.kw

Received August 21 2021; Revised October 04 2021; Accepted for publication October 05 2021.
Corresponding author: S. Roy (sjroy@iitm.ac.in)

Abstract. The flow mechanism and entropy production of a bi-convective, magnetized, radiative nano-liquid flow for an inverted cone considering temperature-sensitive water properties is accomplished numerically. The functional nanomaterial comprises Copper, Alumina in the base liquid, water. The mathematical equations representing the system's physical characteristics are solved numerically by adopting a robust numerical approach for indulgencing non-similar solutions to understand numerous parameters' effect on temperature, velocity, salient gradients, and entropy production. The investigation summarizes that buoyancy force and injection heighten the velocity, and suction, particle percentage, radiation elevate the heat transfer. At the same time, the radiation and Brinkman number enhance the entropy generation. It is also detected from this investigation that the magnetic effect shows dual behaviour in entropy generation.

Keywords: Bi-convection, Water-based nanofluid flows, Temperature-sensitive, Linearization technique, Eentropy production.

1. Introduction

The studies of convective heat transport and flow analysis for a vertical right circular cone attract researchers due to diverse applications in static heat exchangers, nuclear waste extraction, geothermal reservoirs, and various cooling systems. Wang [1] studied the boundary layer flows for a rotating cone with a concentrated heat source. Yih [2] presented a study in porous media for a cone while the surface is maintained either as non-constant surface temperature or non-constant heat flux. Ravindran et al. [3] discussed the injection/suction effects on steady combined convection flow for an inverted cone. Some more significant researches in this regard are quoted in Refs. [4, 5]. Nanofluid (NF) flow for an inverted right circular cone finds several applications in real-life situations like energy storage systems, astrophysics and health care systems. Chamkha and Rashad [6] investigated NFs free convective flow in porous media for an inverted right circular cone. Nadeem et al. [7, 8] presented a theoretical study of third-grade fluid flow from an inverted revolving cone utilizing HAM. Ghalambaz et al. [9] addressed the size (i.e., diameter) and amount (i.e., vol. %) effect of nanoparticles (NPs) on free convection flow considering the thermal conductivity of NF as temperature-dependent. Reddy et al. [10] deliberated a comprehensive analysis of MHD dusty NF flow with heat sink/source and chemical reaction for an inverted cone. Sandeep and Reddy [11] considered the convective transport of magnetohydrodynamic (MHD) NF flow for vertical wedge/cone considering radiation effects. Prabhavathi and others [12] studied the convective heat and mass transport phenomena of water-hosted NF flow using SWCNTs and MWCNTs. They noticed that the increment of heat transport characteristics improves with the rise of NP vol. % and the enhancement pronounced more for SWCNTs. Most recently, Hanif et al. [13] prescribed a numerical study of MHD-hybrid NF flow using the same geometry utilizing Cu-Fe_3O_4-water NF. There are many notable works on this subject and a few of them are cited in [14-19].

There are several real-life applications in applied physical science, biomedicine, and modern devices like MHD-motors, MHD-generators, MHD-pumps, and MHD-sensors, where electrically conducting fluid flow pass through a magnetic field. In such cases, the flow features get affected by the employed magnetic field and the influence depends on the strength and aspect of the field. Reddy and Chamkha [20] presented a numerical study of MHD NFs flow with radiation and chemical effects. They observed that the improvement of the strength of the magnetic and radiation parameter elevate the temperature profile. In contrast, velocity distribution decreases for the first one and increases for the second parameter mentioned above. Raju and others [21] studied unsteady MHD NF flow considering variable viscosity. They used Ti and Ti-alloy (Ti-6Al-4V: 90% Ti, 6% Al, 4% Vanadium) NPs to suspend in water and concluded that Ti-alloy NFs are fruitful for cooling systems. Noor et al. [22] considered MHD and heat source impacts on the NF flow owing to an inclined isothermal plate. Dogonchi et al. [23] deliberated an analysis of Fe_3O_4-water NF flow considering magnetic field-controlled viscosity and discovered that the imposed field is working as a control element.

Published online: October 10 2021

Some other important works in this field are available in [24–29]. Furthermore, radiation affects the attribution of convective heat transport. Chamkha et al. [30] presented an analysis of radiation effects on NF flow filled with porous media. They found that the local heat transport coefficient increases with increased operational parameters such as buoyancy, thermophoresis, radiation, surface temperature, etc. Harun et al. [31] addressed radiative NF flow in porous media for a stretching sheet.

According to thermodynamics, irreversibility occurs in every thermal process. Irreversibility in any thermo-hydrodynamic system occurs due to friction, heat transfer, thermal radiation, dissipation, electrical resistance, chemical reactions, etc. Entropy generation (EG) is a useful tool for examining system irreversibility. Irreversibility in any thermodynamical system increases the amount of lost work and consequently reduces the system's efficiency. To achieve optimum work efficiency in any thermal process, it is essential to minimize the irreversibility, i.e., entropy generation. In this regard, the vital factors have to be found, so that their effect on the entropy generation can be minimized to attain maximum available work. Currently, EG acquires much attention due to its versatile applications in technical and industrial applications as mentioned in the following texts [14, 32]. Rashid et al. [32] displayed the EG minimization in Fe_3O_4 NF flow by a nonlinearly stretching sheet. Nonlinear radiation was taken into account for this study, and they observed that EG rate improves with the increase of Brinkman number (Br) and nanomaterial volume fraction (ϕ), whereas the reverse behaviour of Bejan number (Be) holds. Pordanjani et al. [33] studied the radiation effect on EG and heat transport characteristics of MHD NF flow in a diagonal rectangular chamber. They noticed that by increasing the Rayleigh number (Ra) and radiation parameter (R), the Nusselt number (Nu) and EG increase. Simultaneously, the same effect is observed in the decrease of Hartman number and angle of the magnetic field. Mahian et al. [34] deliberated the EG in a solar collector plate considering the roughness effect, particle size, and various thermophysical models. Their result shows that the increase in ϕ increases the outlet temperature, but the size effect is insignificant, while the case is precisely the opposite for the Nusselt number (Nu). EG increases for the tube roughness but decreases with an increase of ϕ. They also found that using the different models for thermodynamical properties has less effect on EG. Khan et al. [35] presented the EG minimization in radiative MHD casson NF flow from a stretched surface. A numerical study on EG minimization for the nonlinear radiative MHD flow due to moving needle in NF is carried out by Khan et al. [36]. The Built-in-shooting technique is employed in this study. Ibanez et al. [37] analyzed EG in a porous microchannel filled with NF considering the hydromagnetic and radiation effects. There are numerous studies on EG considering radiation and MHD effects and a few of them are cited in [38-42].

Naturally, nanofluid physical characteristics will enjoy the combined effect of host fluid and nanomaterials' physical properties. If the host fluid properties would vary in temperature, then it will not be a misstep to expect that those properties of the NF are also variable in temperature. From Table 1, which is showing the experimental data for water [43], it can be easily observed that viscosity and Prandtl numbers are varying sufficiently in just 10°C temperature difference. So, for water-based nanoliquids, conductivity is intensely sensitive in temperature, and the physical properties are definitely a function of temperature. Work by Das et al. [44] shows that there is only about 2% increase in thermal conductivity of Al_2O_3-water NF at 21°C while the increment is 10.8% at 51°C using only 1% NPs. Moreover, most of the works, till date, are done considering the constant characteristics of water [11-13]. According to the best of authors' knowledge, it is the first project on the evaluation of nanofluid flow characteristics by considering the temperature-sensitive physical characteristics of water. So, by taking into account the physical properties of water, one step forward, this project's primary intent is to analyze the MHD NF flow mechanism, entropy generation and convective heat transport phenomena over an inverted right circular cone with radiation effect. The combined convection effect and surface mass disposal have considered so that the analysis includes a wide range of practical applications. Besides, local entropy generation behaviour is analyzed utilizing Bejan number (Be) and nondimensional local entropy generation (S_G).

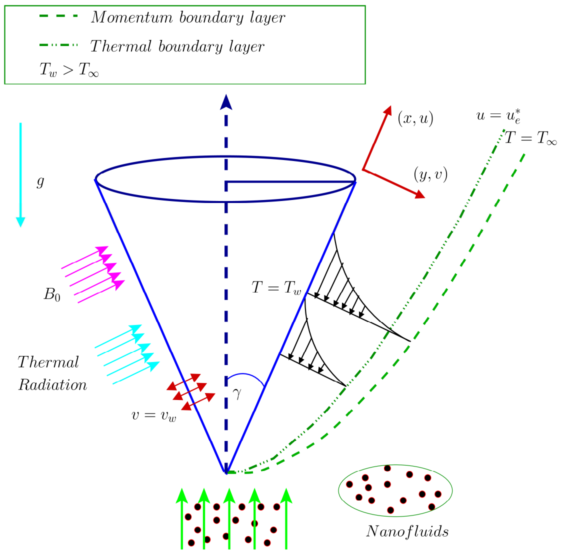

Fig. 1. Flow model and geometrical coordinates of the problem

Table 1. Water thermophysical properties at various temperatures [46].

T(C)	ρ (g. cm^{-3})	C_p (J. 10^7. kg^{-1} K^{-1})	k (erg.10^5.cm^{-1}.s^{-1}.K^{-1})	μ (g.10^{-2}.cm^{-1}.s^{-1})	Pr
0	1.00228	4.2176	0.5610	1.7930	13.48
10	0.99970	4.1921	0.5800	1.3070	9.45
20	0.99821	4.1818	0.5984	1.0060	7.03
30	0.99565	4.1784	0.6154	0.7977	5.12
40	0.99222	4.1785	0.6305	0.6532	4.32
50	0.98803	4.1806	0.6435	0.5470	3.55

Table 2. Nanoparticle and water thermophysical properties [54].

Properties	Water	Copper	Alumina
$C_p (J\ kg^{-1} K^{-1})$	4179	385	765
$\rho\ (kg.\ m^{-3})$	997.1	8933	3970
$k\ (W\ m^{-1} K^{-1})$	0.613	400	40
$\beta \times 10^{-5} K^{-1}$	21	1.67	0.85

2. Mathematical Formulation

Consider a $2D$, steady laminar bi-convective NF flow over an inverted cone where the flow is along the cone generator with $u_e^* = u_\infty x^m$. The x-axis is considered along with the cone generator in flow direction and y-axis is its perpendicular through which surface mass disposal is considered (see Figure 1). The variation in temperature (T) between the wall and fluid is deemed moderate ($< 40°C$), and the fluid motion is regarded as medium velocity. Depending on the data of Table 1, μ (viscosity) and Pr (Prandtl No.) are modeled as below [45]

$$\mu_f(T) = \frac{1}{b_1 + b_2 T} \tag{1}$$

$$Pr(T) = \frac{1}{c_1 + c_2 T} \tag{2}$$

with

$$(b_1\ b_2,\ c_1,\ c_2) = (53.41,\ 2.43,\ 0.068,\ 0.004)$$

The conventional fluid-nanofluid relations for various physical properties, which are valid only for the dilute suspension of fine spherical nanoparticles, given by [46, 47]

$$\mu_{nf}(T,\phi) = \frac{\mu_f(T)}{(1-\phi)^{2.5}} \tag{3}$$

$$\frac{\rho_{nf}(T,\phi)}{\rho_f(T)} = (1-\phi) + \frac{\rho_s}{\rho_f(T)}\phi \tag{4}$$

$$\frac{(C_p\rho)_{nf}(T,\phi)}{(C_p\rho)_f(T)} = (1-\phi) + \frac{(C_p\rho)_s}{(C_p\rho)_f(T)}\phi \tag{5}$$

$$\frac{(\beta\rho)_{nf}(T,\phi)}{(\beta\rho)_f(T)} = (1-\phi) + \frac{(\beta\rho)_s}{(\beta\rho)_f(T)}\phi \tag{6}$$

$$\frac{k_{nf}(T,\phi)}{k_f(T)} = 1 + \frac{3\left(\frac{k_s}{k_f(T)} - 1\right)\phi}{\left(\frac{k_s}{k_f(T)} + 2\right) - \left(\frac{k_s}{k_f(T)} - 1\right)\phi} \tag{7}$$

$$\frac{\sigma_{nf}(T,\phi)}{\sigma_f(T)} = 1 + \frac{3\left(\frac{\sigma_s}{\sigma_f(T)} - 1\right)\phi}{\left(\frac{\sigma_s}{\sigma_f(T)} + 2\right) - \left(\frac{\sigma_s}{\sigma_f(T)} - 1\right)\phi} \tag{8}$$

where the terms ϕ, μ_{nf}, μ_f, ρ_{nf}, ρ_f, ρ_s, $(C_p)_{nf}$, $(C_p)_f$, $(C_p)_s$, β_{nf}, β_f, β_s, k_{nf}, k_f, k_s, σ_{nf}, σ_f, σ_s are all given in the appendix.

One can easily observe from Table 1 that the variation of ρ and C_p of water in temperature within the moderate temperature difference ($< 40°C$) are less than 1%. A similar consequence can be verified through the correlations listed above for nanofluid too. Suppose ρ_{f_1}, ρ_{f_2} and ρ_{nf_1}, ρ_{nf_2} be the densities of water and nanofluids at two different temperature $T_0^o C < T_1^o C$, respectively, both lies within the range ($0 - 50°C$) and $(T_1 - T_0)^{\circ} C < 40°C$.

Clearly,

$$\frac{\rho_{f_1}(T) - \rho_{f_2}(T)}{\rho_{f_1}(T)} \le 0.01$$

Again,

$$\rho_{nf_1}(T,\phi) = \rho_{f_1}(T)(1-\phi) + \rho_s\phi$$
$$\rho_{nf_2}(T,\phi) = \rho_{f_2}(T)(1-\phi) + \rho_s\phi$$

Therefore

$$\frac{\rho_{nf_1}(T,\phi)-\rho_{nf_2}(T,\phi)}{\rho_{nf_1}(T,\phi)}=\frac{(1-\phi)(\rho_{f_1}-\rho_{f_2})}{\rho_{nf_1}(T,\phi)}=\frac{\dfrac{(\rho_{f_1}(T)-\rho_{f_2}(T))}{\rho_{f_1}(T)}}{1+\dfrac{\phi}{1-\phi}\dfrac{\rho_s}{\rho_{f_1}}}\leq\frac{0.01}{1+\dfrac{\phi}{1-\phi}\dfrac{\rho_s}{\rho_{f_1}}}\leq 0.01$$

Since $0\leq\phi<1\Rightarrow\phi/(1-\phi)\geq 0$ and therefore $1+\phi\rho_s/(1-\phi)\rho_{f_1}\geq 1$. This proves that the variation in nanofluid density is less than 1% in the said temperature range and in a similar way, using the same type of simple calculations, it can be shown that variation in $(C_p)_{nf}$ is less than 1% too and therefore $(\rho)_{nf}$ and $(C_p)_{nf}$ both can be treated as constant (Values are given in Table 2).

But contrary to the above, μ and Pr of nanofluid are non-constant properties i.e., variable in temperature since there are significant variations in μ and Pr for water.

The governing flow equations are as follows [2-3, 48]:

$$\vec{\nabla}.\vec{q}=0 \qquad : \qquad \vec{q}\equiv(u,v) \tag{9}$$

$$\vec{q}.\vec{\nabla}u=u_e^*\frac{du_e^*}{dx}+\frac{1}{\rho_{nf}}\frac{\partial}{\partial y}\left(\mu_{nf}\frac{\partial u}{\partial y}\right)+g\frac{(\rho\beta)_{nf}\cos\gamma}{\rho_{nf}}[T-T_\infty]-\frac{\sigma_{nf}B_0^2}{\rho_{nf}}(u-u_e^*) \tag{10}$$

$$\vec{q}.\vec{\nabla}T=\frac{1}{(\rho C_p)_{nf}}\frac{\partial}{\partial y}\left(k_{nf}\frac{\partial T}{\partial y}\right)-\frac{1}{(\rho C_p)_{nf}}\frac{\partial q_r}{\partial y} \tag{11}$$

where

$$q_r=-\frac{4\sigma^*}{3k^*}\frac{\partial T^4}{\partial y}$$

and the constraints:

$$T=T_w;\ u=0;\ v=v_w \quad at\, y=0 \tag{12}$$

$$T\to T_\infty;\ u\to u_e^*; \quad as\, y\to\infty \tag{13}$$

Utilizing the following congenial transformations:

$$\xi=\frac{1}{L}\left(\frac{2}{(m+1)}\frac{\nu_\infty x}{u_e^*}\right)^{\frac{1}{2}}; \qquad \eta=y\left(\frac{(m+1)}{2}\frac{u_e^*}{\nu_\infty x}\right)$$

$$\psi(x,y)=\left(2(m+1)^{-1}\nu_\infty x u_e^*\right)^{\frac{1}{2}}f$$

$$\frac{\partial\psi}{\partial x}=-v,\ \frac{\partial\psi}{\partial y}=u,\ f_\eta=F$$

$$u=u_e^*F,\ v=-\left(\frac{1}{(m+1)}\frac{u_e^*\nu_\infty}{2x}\right)^{\frac{1}{2}}\left((1+m)f+(1-m)(\xi f_\xi-\eta F)\right)$$

Eqs. (10)-(11) reduces to the following nondimensional forms:

$$\frac{\partial}{\partial\eta}\{NF_\eta\}+S_1\frac{2\lambda G}{(1+m)}-K_1S_1Ma^2\xi^2(F-1)+S_2\left(\frac{2m}{(1+m)}(1-F^2)+fF_\eta-\left(\frac{1-m}{1+m}\right)\xi(FF_\xi-f_\xi F_\eta)\right)=0 \tag{14}$$

$$\frac{N}{Pr}\left(\frac{P_1+P_2G}{P_3+P_4G}+R\right)G_{\eta\eta}+\frac{\partial}{\partial\eta}\left(\frac{N}{Pr}P_5\right)G_\eta+S_3\left(fG_\eta-\left(\frac{1-m}{1+m}\right)\xi(FG_\xi-f_\xi G_\eta)\right)=0 \tag{15}$$

and

$$\begin{bmatrix}F\\G\end{bmatrix}_{\eta=0}=\begin{bmatrix}0\\1\end{bmatrix};\ \begin{bmatrix}F\\G\end{bmatrix}_{\eta=\eta_\infty}=\begin{bmatrix}1\\0\end{bmatrix} \tag{16}$$

Here $\lambda=g\beta_f\cos\gamma\Delta T x/u_e^{*2}$, $Ma=\sigma_f B_0^2L^2/\rho_f\nu_\infty$ and $R=16\sigma^* T_\infty^3/3k^*k_f$ are the dimensionless parameters P_1,P_2,P_3,P_4 and K_1,S_1,S_2,S_3 are constant coefficients, which are defined in appendix.

The surface mass disposal is defined in the following form:

$$v_w=\frac{\nu_\infty}{\xi L}\left[f_w+\left(\frac{1-m}{1+m}\right)\xi(f_\xi)_w\right]$$

$$f_w + \left(\frac{1-m}{1+m}\right)\xi(f_\xi)_w = -\left(\frac{\upsilon_w L}{\nu_\infty}\right)\xi = A\xi$$

where $A = -\upsilon_w L / \nu_\infty$ is the dimensionless surface mass disposal parameter.

The gradients of physical interest are:

1. Skin friction:

$$C_{fx} = \frac{\mu_{nf}\left(\frac{\partial u}{\partial y}\right)_{y=0}}{\frac{1}{2}\rho_f u_e^{*2}} = \frac{2}{(1-\phi)^{2.5}}\sqrt{\frac{m+1}{2}}Re_x^{-\frac{1}{2}}F_\eta(\xi,0)$$

$$\therefore Re_x^{\frac{1}{2}}C_{fx} = \frac{2}{(1-\phi)^{2.5}}\sqrt{\frac{m+1}{2}}F_\eta(\xi,0)$$

2. Heat transfer (Nusselt No.):

$$Nu_x = -\frac{xk_{nf}\left(\frac{\partial T}{\partial y}\right)_{y=0}}{k_f(T_w - T_\infty)} = -\sqrt{\frac{m+1}{2}}Re_x^{\frac{1}{2}}\left[\frac{P_1+P_2}{P_3+P_4}\right]G_\eta(\xi,0)$$

$$Re_x^{-\frac{1}{2}}Nu_x = -\sqrt{\frac{m+1}{2}}\left[\frac{P_1+P_2}{P_3+P_4}\right]G_\eta(\xi,0)$$

3. Entropy Generation

The entropy model for hydromagnetic NF flow with radiation effect can be written as [49-51]:

$$S_{gen} = \underbrace{\frac{1}{T^2}\left(k_{nf}\left(\frac{\partial T}{\partial y}\right)^2 + \frac{16T_\infty^3}{3k^*}\left(\frac{\partial T}{\partial y}\right)^2\right)}_{HTI} + \underbrace{\frac{\mu_{nf}}{T}\left(\frac{\partial u}{\partial y}\right)^2 + \frac{\sigma_{nf}B_0^2}{T}u}_{FFI}$$

HTI (heat transfer irreversibility) is the local entropy generation due to heat transfer and the entropy generation due to Joule effect and fluid friction are summed up as FFI (fluid friction irreversibility). The local entropy generation S_{gen} is made non-dimensional (S_G) using the characteristic entropy rate $S_0 = \Delta T^2 k_f / L^2 T_\infty^2$ i.e., $S_G = S_{gen} / S_0 = N_1 + N_2$ where

$$N_1 = \frac{HTI}{S_0} = \left[\frac{P_1 + P_2 G}{P_3 + P_4 G} + R\right]\frac{G_\eta^2}{\xi^2(1+\Omega G)}$$

$$N_2 = \frac{FFI}{S_0} = \left[\frac{F_\eta^2}{(1-\phi)^{2.5}(1+a_1 G)} + \xi^2 K_1 (Ma)^2 F^2\right]\frac{Br}{\xi^2\Omega(1+\Omega G)}$$

where $\Omega = \Delta T / T_\infty$ and $Br = \mu_f u_e^{*2} / k_f \Delta T$ is Brinkman number. Bejan number is a useful tool to calculate the energy distribution and is defined by

$$Be = \frac{N_1}{N_1 + N_2}$$

Be lies in the range $0 \le Be \le 1$. $Be = 0$ suggests that HTI is beaten by FFI and $Be =$ 1 implies that FFI is dominant by HTI. The equal contribution of both the irreversibilities due to heat transform and fluid friction refers to $Be =$ 0.5.

4. Numerical Methods

To solve the transformed Eqs. (14) to (16), the following order of numerical approaches have been employed: (i) Quasilinearization [52], (ii) Finite difference, (iii) Varga algorithm [53]. In this procedure, step-(i) produces

$$A_1^{(k)}F_{\eta\eta}^{(k+1)} + A_2^{(k)}F_\eta^{(k+1)} + A_3^{(k)}F_\xi^{(k+1)} + A_4^{(k)}F^{(k+1)} + A_5^{(k)}G_\eta^{(k+1)} + A_6^{(k)}G^{(k+1)} = A_7^{(k)} \tag{17}$$

$$M_1^{(k)}G_{\eta\eta}^{(k+1)} + M_2^{(k)}G_\eta^{(k+1)} + M_3^{(k)}G_\xi^{(k+1)} + M_4^{(k)}G^{(k+1)} + M_5^{(k)}F^{(k+1)} = M_6^{(k)} \tag{18}$$

and

$$\begin{bmatrix} F^{(k+1)} \\ G^{(k+1)} \end{bmatrix}_{\eta=0} = \begin{bmatrix} 0 \\ 1 \end{bmatrix}; \begin{bmatrix} F^{(k+1)} \\ G^{(k+1)} \end{bmatrix}_{\eta=\eta_\infty} = \begin{bmatrix} 1 \\ 0 \end{bmatrix} \tag{19}$$

At first, the nonlinear coupled partial differential equations were replaced by an iterative sequence of linear partial differential equations following quasilinearization technique. The resulting sequence of linear partial differential equations is expressed as difference equations using stable finite difference scheme to produce convergent numerical solutions. The linear system (17)-(18) is displayed for the unknown with superscript (k+1). All the coefficients $A_1, M_1, A_2, M_2, A_3, M_3, A_4, M_4, A_5, M_5, A_6, M_6, A_7$ are defined in Appendix. Step-(ii) is being used to convert Eqs. (17-18) into the Block matrix system, and finally, the resultant structure has been solved using Step-(iii). A proficient convergence criterion has been employed throughout the calculations to get numerically feasible solutions. Here m, the exponent power of the outer flow field is considered ½ to get λ as a constant. Assigning $\phi=0$, $Ma=0$, $R=0$, the transformed Eqs. (14-15) become similar with those in Ravindran et al. [3].

5. Results with Discussion

The numerical results presented through sketches depict various operational parameters of concern on the common profiles. To check the preciseness of this present numerical scheme, graphical comparisons have been made with Ravindran et al. [3] for $\phi=0$, $m=0$, $\lambda=0$, $Ma=0$, $R=0$ and $A=0$, and displayed in Fig. 2, and they are in a friendly match up. Al_2O_3 and Cu NPs are taken as working nanoparticle.

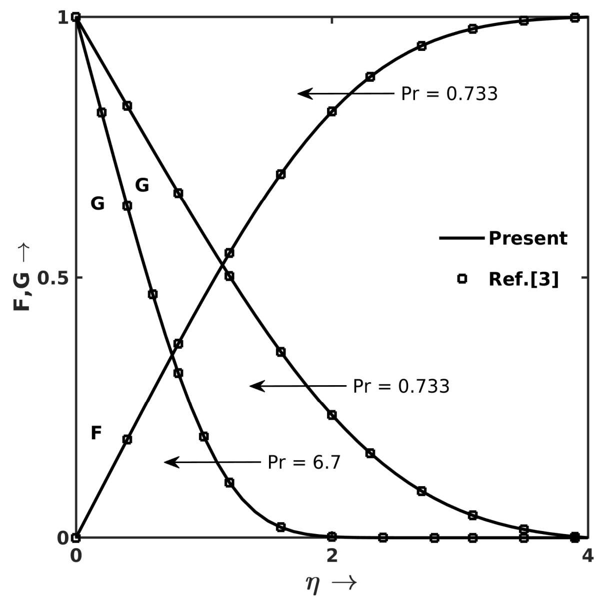

Fig. 2. Results Verification

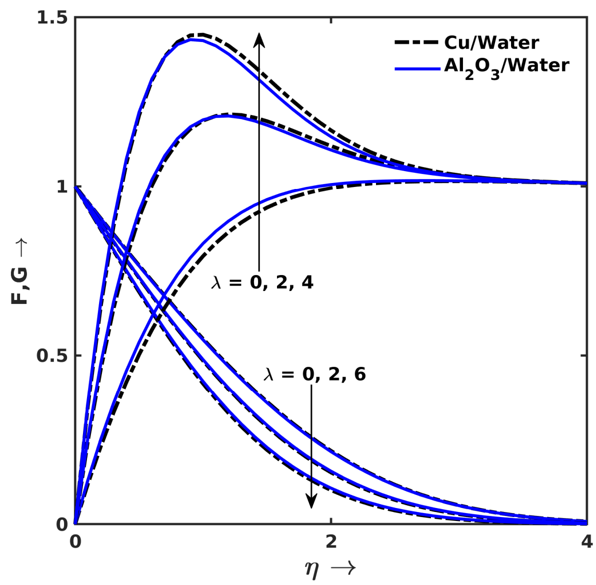

Fig. 3. λ effect on F, G

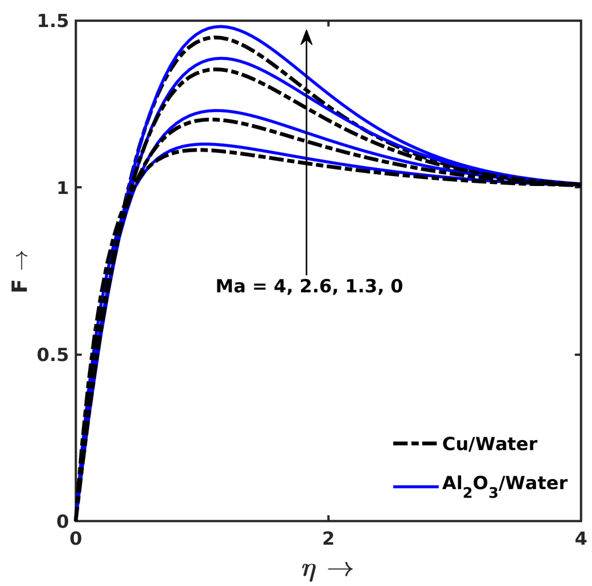

Fig. 4. Ma effect on F

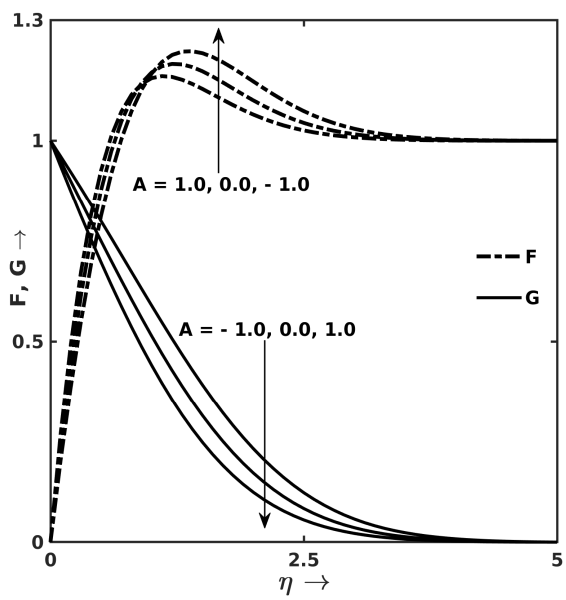

Fig. 5. A effect on F, G

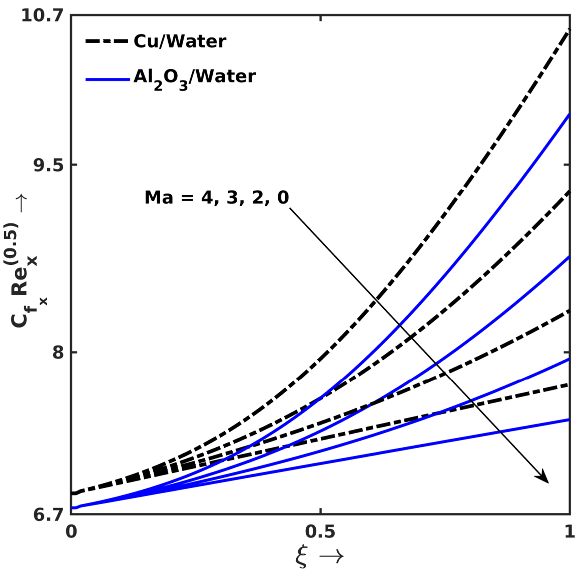

Fig. 6. *Ma* effect on C_f

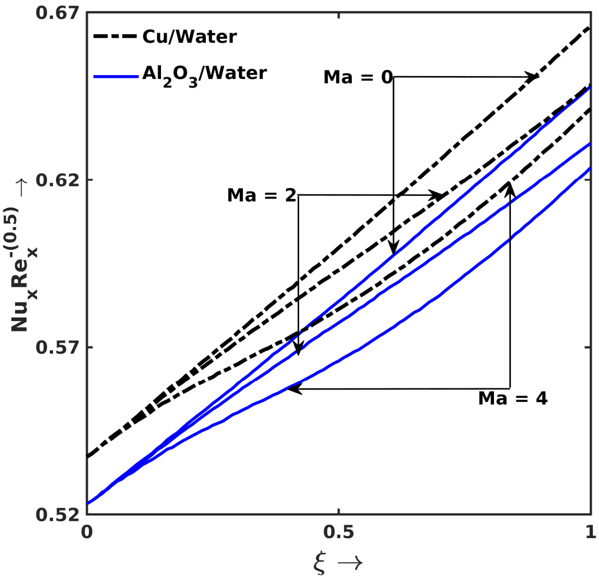

Fig. 7. *Ma* effect on *Nu*

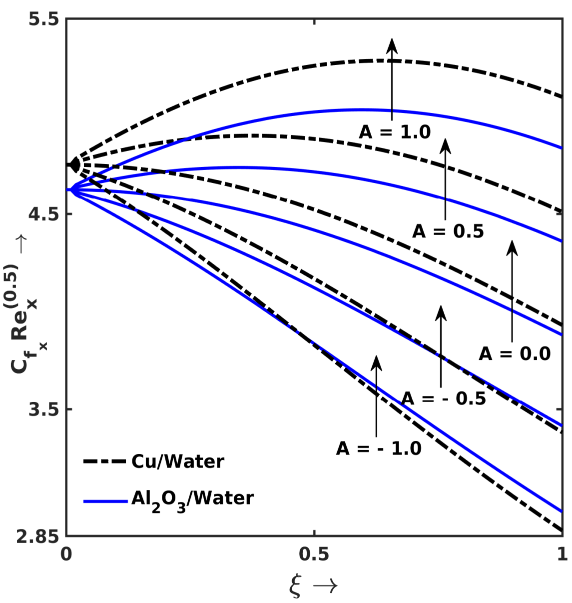

Fig. 8. *A* effect on C_f

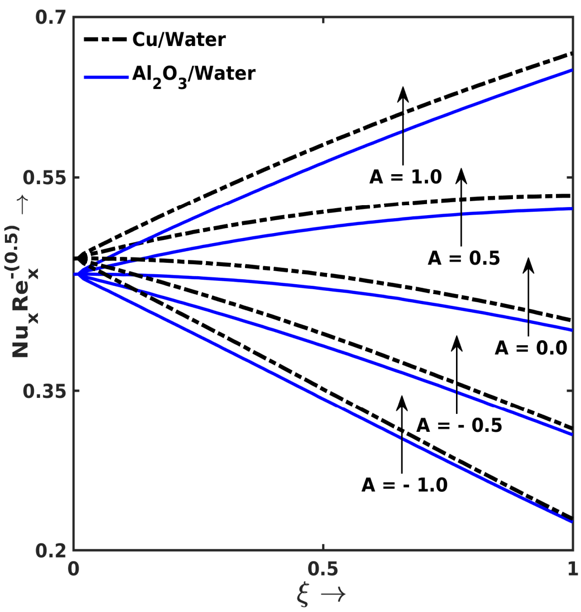

Fig. 9. *A* effect on *Nu*

Buoyancy creates an additive pressure force, and increased buoyancy force increases the flow velocity. The flow velocity is affected conspicuously in the variation of λ as shown graphically in Fig. 3. Even one can observe from the specific graph (Fig. 3) that there is an overshoot in F for some higher $\lambda(2,4)$. As the buoyancy force's strength rises, the free convection starts to dominate the forced convection. In such cases, the velocity near the vicinity of the wall becomes higher, and overshoot occurs. Accordingly, for large λ the flow speed increases sufficiently near the surface, the flow quickly attained its free flow velocity and finally, the momentum boundary layer (BL) becomes thinner.

Figure 4 elucidates the magnetic parameter (Ma) on F. Visual evidence in Fig. 4 shows that F decreases with Ma. The physical reason behind this is that an increase in Ma creates a force, named Lorentz force, which has the characteristics to restrict the fluid movement within the BL. Since the parameter Ma appears on momentum equation, the effects of Ma on temperature profile is less and temperature profile vary within 5% due to the increase of Ma from 0 to 4. The graph is not displayed to brief the manuscript.

Figure 5 characterizes the influence of mass disposal at the surface on both the profiles F and G. Results show that the velocity field is of smaller magnitude for suction ($A>0$) and higher for injection ($A<0$), but its gradient near the wall is higher for $A>0$. This is because suction takes away the slowed down fluids flowing in the cone wall's vicinity, and the flow tries to sustain the same velocity level near the surface. Moreover, blowing fluids into the BL region increases the liquid's mass density, and as a result, the flow slows down. In the temperature profile, the curves representing suction ($A>0$) are stiffer than those for injection ($A<0$).

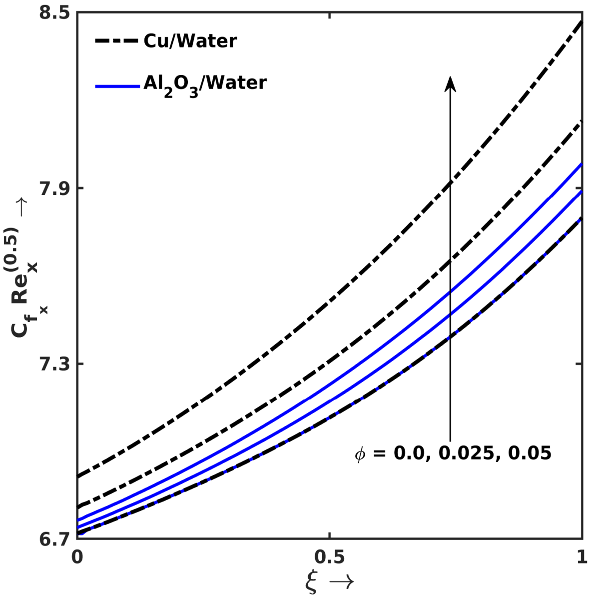

Fig. 10. ϕ effect on C_f

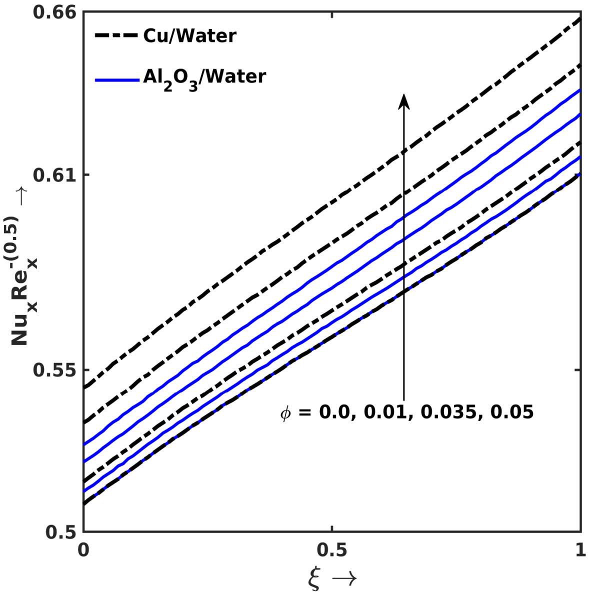

Fig. 11. ϕ effect on Nu

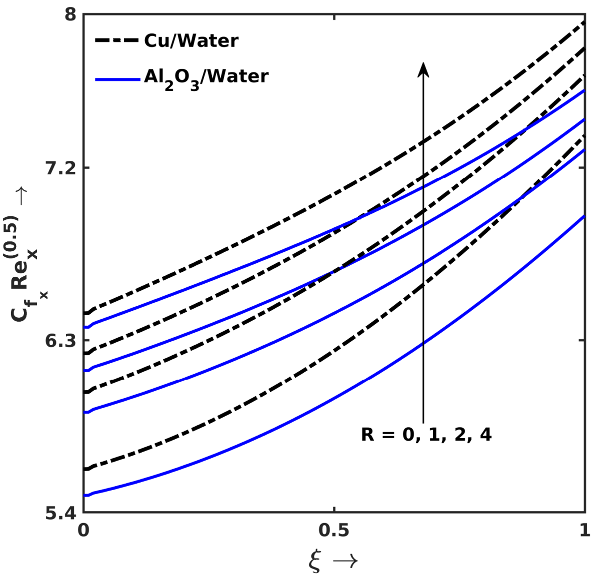

Fig. 12. R effect on C_f

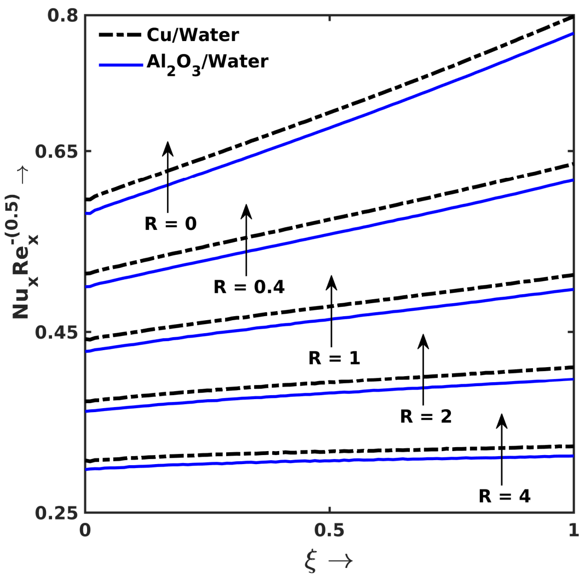

Fig. 13. R effect on Nu

The coefficient of skin friction increases with Ma, but the heat transfer coefficient decreases as displayed in Figs. 6-7. The magnetic field works as an external force to attract the NPs, which leads to faster motion. Consequently, $C_{fx}Re_x^{1/2}$ becomes higher due to the faster moving fluids for higher Ma. Moreover, this increased friction produces significant heat and enhances the adjacent fluid temperature, interrupting heat convection.

The graphical evidences presented through Figs. 8-9 indicate that both $C_{fx}Re_x^{1/2}$ and $Re_x^{-1/2}Nu_x$ increase when suction is present and the result is reverse when injection is present in the flow field. At $\xi = 1$, $C_{fx}Re_x^{1/2}$ increases by $12\%, 15\%$ when A rises from 0 to 0.5 and decreases by $12\%, 14\%$ when A decadences from 0 to -0.5 for Al_2O_3/H_2O and Cu/H_2O, respectively. Similarly, at $\xi = 1$, $Re_x^{-1/2}Nu_x$ increases by $29\%, 28\%$ when A rises from 0 to 0.5 and decreases by $24\%, 24\%$ when A decadences from 0 to -0.5 for Al_2O_3/H_2O and Cu/H_2O, respectively.

Figures 10-11 highlight the features of $C_{fx}Re_x^{1/2}$ and $Re_x^{-1/2}Nu_x$ against ϕ. It is clear from the graphs that both the coefficients increase in the enhancement of the particle volume percentage (ϕ). It is quite predictive because the main motto of suspending NPs was to enrich the conductivity (thermal). Current results show that the conductivity (thermal) presented through $Re_x^{-1/2}Nu_x$ increases with a higher percentage of ϕ. But, the suspended NPs enhance the fluid mass density too, which strengthening the wall friction. When the NP concentration percentage (ϕ) rises from 0% to 2.5% and 5%, it is observed that at $\xi = 1$ the increments in $C_{fx}Re_x^{1/2}$ are 4% and 9%, respectively, for Cu NPs. Also, at $\xi = 1$ the percentages of increment for $Re_x^{-1/2}Nu_x$ are almost 4% and 8% when ϕ rises from 0% to 3.5%, and 5%, respectively.

Figures 12 – 13 depict the impact of R on $C_{fx}Re_x^{1/2}$. Figure 12 shows that $C_{fx}Re_x^{1/2}$ improve with the increment of R. Basically, an increment in R enhances the system's internal energy and as a result, $C_{fx}Re_x^{1/2}$ increases. In contrast, $Re_x^{-1/2}Nu_x$ is diminished for higher R because the enhanced internal energy improves the system's temperature, as portrayed in Fig. 13.

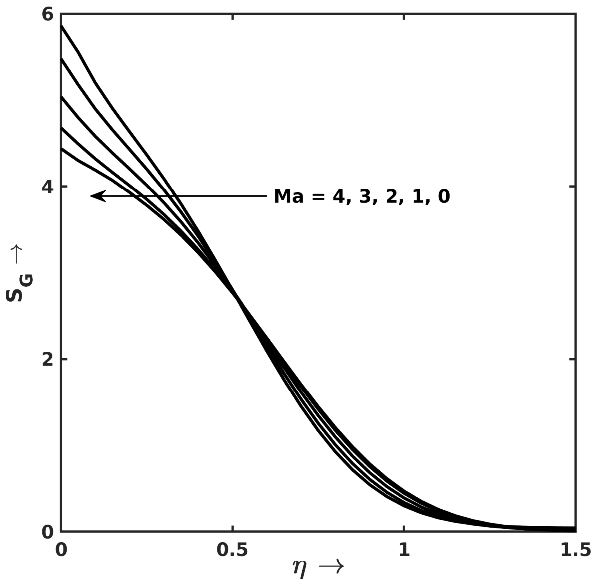

Fig. 14. Ma effect on S_G

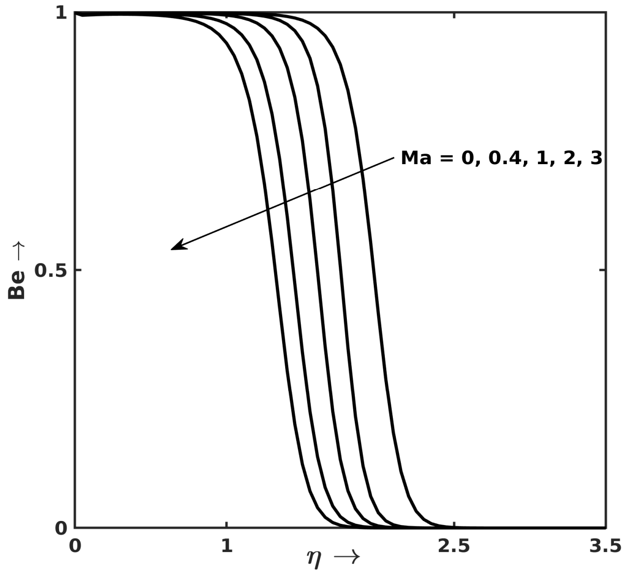

Fig. 15. Ma effect on Be

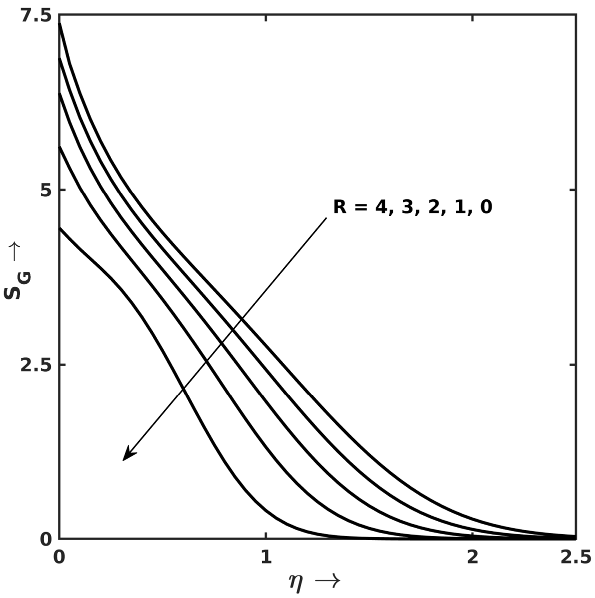

Fig. 16. R effect on S_G

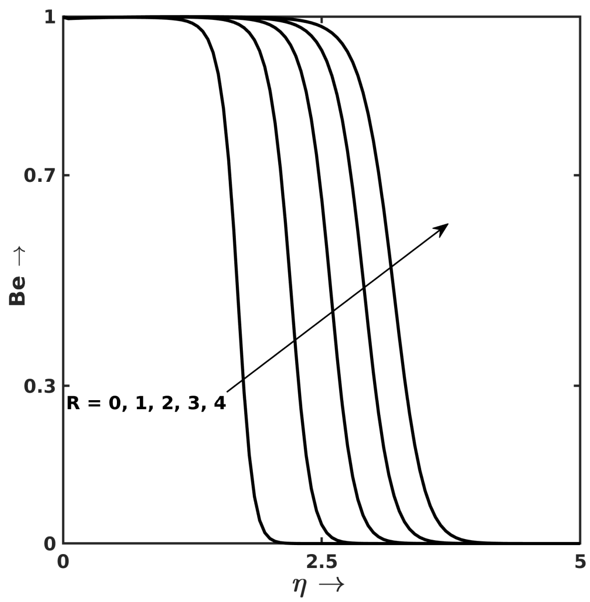

Fig. 17. R effect on Be

Overall, quantitative results in compact form are presented in Table 3 for better understanding of the variations of numerical results as displayed in Figs. 6 – 13. This section present results with Cu as working nanoparticle.

Figures 14-18 are plotted to characterize the effects of different parameters Ma, ϕ, R, Br on S_G and Be. The impact of the Magnetic parameter Ma on S_G is shown through Fig. 14. It depicts that S_G has a higher value for the higher magnitude of Ma within the range $0 \le \eta < 0.5$, but the graph sharply drops for $\eta > 0.5$, and S_G shows lower magnitudes for higher Ma. The significance of a magnetic fields' presence in a flow is that the dissipative heat energy is forced to convert into thermal diffusion. So, when the strength of Ma rises, the heat energy due to the friction at the surface gets transferred into the fluid as thermal diffusion near the wall. In explicit form, it can be described as; HTI overtakes FFI and Be remains almost unit near the wall as depicted in Fig. 15. But away from the surface, increment in Ma rises the share of FFI in total S_G and as a result, Be shows lower magnitude. Figures 16-17 have sketched to visualize the variation of nonlinear thermal radiation (R) on S_G and Be. The radiation effect R added some external energy to the internal energy of the system of the concerned flow field and the total energy grows up, as shown in Fig. 16. Being enriched by the external energy, HTI beats FFI, and the impact is more prominent for the high magnitude of R as evidenced in Fig. 17. Figure 18 characterizes the impact of $Br\Omega^{-1}$ on Be. Near the cone wall, viscous heating is less compared to heat transferred due to conduction of molecules. For higher Br, i.e., for viscous heating, the heat transfer component HTI takes over FFI. On the contrary, the heat transfer component HTI gets reduced in the flow away from the cone surface, as supported by Fig. 18 which shows that Be lines are lifted for lower $Br\Omega^{-1}$.

Table 3. Quantitative representation of numerical results.

	$C_{fx}Re_x^{1/2}$		$Re_x^{-1/2}Nu_x$	
	Al_2O_3	Cu	Al_2O_3	Cu
Ma = 0	7.1040	7.3008	0.5843	0.6003
1	7.1333	7.3386	0.5821	0.5980
2	7.2561	7.4898	0.5772	0.5929
3	7.5123	7.7955	0.5726	5882
4	7.8978	8.2440	0.5692	0.5849
A = -1.0	3.8248	3.8263	0.3425	0.3517
-0.5	4.0874	4.1338	0.3891	0.3999
0.0	4.3603	4.4593	0.4411	0.4538
0.5	4.6389	4.7969	0.4980	0.5125
1.0	4.9215	5.1432	0.5604	0.5767
ϕ = 0.0	7.1655	7.1655	0.5598	0.5598
0.025	7.2213	7.3651	0.5707	0.5804
0.05	7.2798	7.5750	0.5815	0.5887
R = 0.0	6.0766	6.3366	0.6773	0.6941
1.0	6.5025	6.7274	0.4637	0.4778
2.0	6.7073	6.9179	0.3813	0.3935
3.0	6.8318	7.0326	0.3360	0.3467
4.0	6.9149	7.1087	0.3069	0.3168

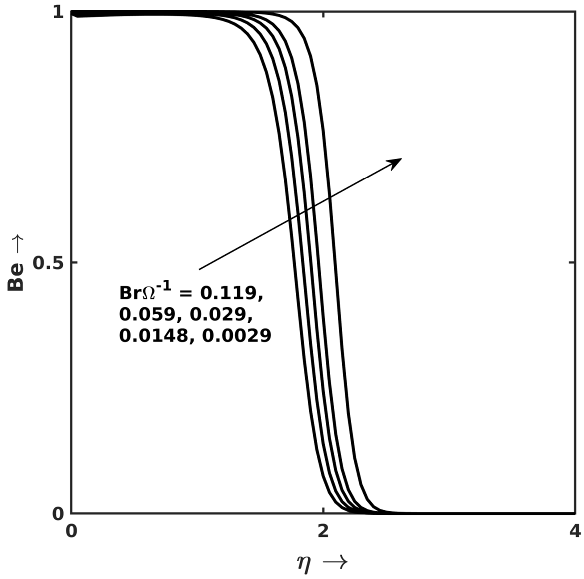

Fig. 18. *Br* effect on *Be*

6. Conclusions

The sway of emerging parameters in this study brought the following conclusive remarks:

i. Velocity increases for positive λ. The higher intensity of λ causes a stiffer boundary layer. With the increase of λ, overshoot increases and maximum velocity comes close to the surface. For $\lambda=2,4$, Cu/H_2O NF flow have maximum overshoots by 20% and 43% which take place, respectively, at $\eta=1.2, 0.9$.

ii. About 19% reduction is detected in flow velocity for Al_2O_3/H_2O NFs flow field at η = 0.9 with hydro-magnetic parameter Ma of strength 4, compared with the flow field without any magnetic effect.

iii. It is also observed that increasing Ma from 0 to 4 diminish $Re_x^{-1/2}Nu_x$ by about 4% whereas it rises $Re_x^{\frac{1}{2}}C_{f_x}$ by about 37%.

iv. Uniform suction ($A>0$) at the surface absorbs slowed down fluids of low momentum. Consequently, this leads to an increment in the fluid motion adjacent to the wall.

v. The suction effect of strength $A=0.5$ enhances the heat transfer coefficient as well as friction coefficient by about 28% and 12%, respectively. On the other hand, injecting fluids within the flow ($A=-0.5$) decreases both the coefficients $C_{fx}Re_x^{1/2}$ and $Re_x^{-1/2}Nu_x$ by about 12% and 24%, respectively.

vi. Increase in ϕ enhances $Re_x^{-1/2}Nu_x$. Even in particular, at $\xi=1.0$, mixing only 5% Cu-NP improves the coefficient heat transfer by about 8%, while Al_2O_3-NPs could hardly enhance $Re_x^{-1/2}Nu_x$ by only 4.2%.

vii. Increment in Ma, R, ϕ and Br generates more entropy, especially within the cone wall's vicinity.

viii. S_G shows dual behavior for Ma. The increase in Ma displays higher S_G within the range $0 \le \eta < 0.5$, but the graph sharply drops near $\eta=0.5$, and S_G shows lower magnitudes for higher Ma.

ix. An increment in R from $0-2$ and $0-4$ elevates S_G by nearly 43% and 70%, respectively, at $\eta=0.5$.

Author Contributions

All authors are equally contributed.

Acknowledgments

Not applicable.

Conflict of Interest

The authors declared no potential conflicts of interest concerning the research, authorship, and publication of this article.

Funding

The authors received no financial support for the research, authorship, and publication of this article.

Data Availability Statements

The datasets generated and/or analyzed during the current study are available from the corresponding author on reasonable request.

Nomenclature

B_0	Magnetic parameter
C_p	Specific Heat capacitance
f, F	Non-dimensional stream function and velocity, respectively
g	Gravity
G	Non-dimensional temperature
k	Conductivity (thermal)
L	Reference length
m	Non-dimensional pressure gradient
Ma	Non-dimensional magnetic parameter
R	Non-dimensional radiation parameter
Re	Reynolds number
v, u	Velocity components in the y and x direction
Greek Symbols	
β	Volumetric expansion coefficient (thermal)
λ	Buoyancy
ξ	Stream-wise coordinate
η	Perpendicular coordinate to ξ
ρ	Density
σ	Conductivity (electrical)
ϕ	Nanoparticle percentage in NF
ψ	Stream function
Subscripts	
e	Conditions at the edge of BL
w, ∞	Conditions at the surface and infinity, respectively
nf	Nanofluid
f	Base Liquid
s	Solid
Superscripts	
k	Iteration number
Abbreviations	
NF	Nanofluid
NP	Nanoparticles
MHD	Magnetohydrodynamics
CNT	Carbon nanotubes
BL	Boundary layer

References

[1] Wang, C.Y., Boundary layers on rotating cones, discs and axisymmetric surfaces with a concentrated heat source, *Acta Mechanica*, 81(3), 1990, 245-251.
[2] Yih, K.A., Mixed convection about a cone in a porous medium: the entire regime, *International Communications in Heat and Mass Transfer*, 26(7), 1999, 1041-1050.
[3] Ravindran, R., Roy, S., Momoniat, E., Effects of injection (suction) on a steady mixed convection boundary layer flow over a vertical cone, *International Journal of Numerical Methods for Heat & Fluid Flow*, 19(3/4), 2009, 432 - 444.
[4] Daskalakis, J.E., Mixed free and forced convection in the incompressible boundary layer along a rotating vertical cylinder with fluid injection, *International Journal of Energy Research*, 17(8), 1993, 689-695.
[5] Ravindran, R. and Ganapathirao, M., Non-uniform slot suction/injection into mixed convection boundary layer flow over vertical cone, *Applied Mathematics and Mechanics*, 34(11), 2013, 1327-1338.
[6] Chamkha, A.J. and Rashad, A.M., Natural convection from a vertical permeable cone in a nanofluid saturated porous media for uniform heat and nanoparticles volume fraction fluxes, *International Journal of Numerical Methods for Heat & Fluid Flow*, 22(8), 2012, 1073- 1085.
[7] Nadeem, S., Theoretical Investigation of MHD nanofluid flow over a rotating cone: an optimal solutions, *Information Sciences Letters*, 3(2), 2014, 55-62.
[8] Nadeem, S. and Saleem, S., Analytical study of third grade fluid over a rotating vertical cone in the presence of nanoparticles, *International Journal of Heat and Mass Transfer*, 85, 2015, 1041-1048.
[9] Ghalambaz, M., Behseresht, A., Behseresht, J. and Chamkha, A., Effects of nanoparticles diameter and concentration on natural convection of the Al2O3–water nanofluids considering variable thermal conductivity around a vertical cone in porous media, *Advanced Powder Technology*, 26(1), 2015, 224-235.
[10] Reddy, J.V.R., Sugunamma, V., Sandeep, N. and Chakravarthula, S.K., Chemically reacting MHD dusty nanofluid flow over a vertical cone with non-uniform heat source/sink, *Walailak Journal of Science and Technology (WJST)*, 14(2), 2017, 141-156.
[11] Sandeep, N. and Reddy, M.G., Heat transfer of nonlinear radiative magnetohydrodynamic Cu-water nanofluid flow over two different geometries, *Journal of Molecular Liquids*, 225, 2017, 87-94.
[12] Prabhavathi, B., Reddy, P.S. and Vijaya, R.B., Heat and mass transfer enhancement of SWCNTs and MWCNTs based Maxwell nanofluid flow over a vertical cone with slip effects, *Powder Technology*, 340, 2018, 253-263.

[13] Hanif, H., Khan, I. and Shafie, S., Heat transfer exaggeration and entropy analysis in magneto-hybrid nanofluid flow over a vertical cone: a numerical study, *Journal of Thermal Analysis & Calorimetry*, 141(5), 2020, 2001-2017.
[14] Zeeshan, A., Ellahi, R. and Hassan, M., Magnetohydrodynamic flow of water/ethylene glycol based nanofluids with natural convection through a porous medium, *The European Physical Journal Plus*, 129(12), 2014, 1-10.
[15] Reddy, P.S. and Chamkha, A.J., Influence of size, shape, type of nanoparticles, type and temperature of the base fluid on natural convection MHD of nanofluids, *Alexandria Engineering Journal*, 55(1), 2016, 331-341.
[16] Reddy, M.G. and Sandeep, N., Computational modelling and analysis of heat and mass transfer in MHD flow past the upper part of a paraboloid of revolution, *The European Physical Journal Plus*, 132(5), 2017, 1-18.
[17] Dogonchi, A.S., Asghar, Z. and Waqas, M., CVFEM simulation for Fe3O4-H2O nanofluid in an annulus between two triangular enclosures subjected to magnetic field and thermal radiation, *International Communications in Heat and Mass Transfer*, 112, 2020, 104449.
[18] Dogonchi, A.S., Waqas, M., Seyyedi, S.M., Hashemi-Tilehnoee, M. and Ganji, D.D., A modified Fourier approach for analysis of nanofluid heat generation within a semi-circular enclosure subjected to MFD viscosity, *International Communications in Heat and Mass Transfer*, 111, 2020, 104430.
[19] Sadeghi, M.S., Tayebi, T., Dogonchi, A.S., Nayak, M.K. and Waqas, M., Analysis of thermal behavior of magnetic buoyancy-driven flow in ferrofluid–filled wavy enclosure furnished with two circular cylinders, *International Communications in Heat and Mass Transfer*, 120, 2021, 104951.
[20] Reddy, P.S. and Chamkha, A., Heat and mass transfer analysis in natural convection flow of nanofluid over a vertical cone with chemical reaction, *International Journal of Numerical Methods for Heat & Fluid Flow*, 27(1), 2017, 2-22.
[21] Raju, C.S.K., Sandeep, N. and Sugunamma, V., Unsteady magneto-nanofluid flow caused by a rotating cone with temperature dependent viscosity: a surgical implant application, *Journal of Molecular Liquids*, 222, 2016, 1183-1191.
[22] Noor, N.F.M., Abbasbandy, S. and Hashim, I., Heat and mass transfer of thermophoretic MHD flow over an inclined radiate isothermal permeable surface in the presence of heat source/sink, *International Journal of Heat and Mass Transfer*, 55(7-8), 2012, 2122-2128.
[23] Dogonchi, A.S., Waqas, M., Gulzar, M.M., Hashemi-Tilehnoee, M., Seyyedi, S.M. and Ganji, D.D., Simulation of Fe_3O_4-H_2O nanoliquid in a triangular enclosure subjected to Cattaneo–Christov theory of heat conduction, *International Journal of Numerical Methods for Heat & Fluid Flow*, 29(11), 2019, 4430-4444.
[24] Turkyilmazoglu, M., Exact analytical solutions for heat and mass transfer of MHD slip flow in nanofluids, *Chemical Engineering Science*, 84, 2012, 182-187.
[25] Mondal, H., Mishra, S., Kundu, P.K. and Sibanda, P., Entropy generation of variable viscosity and thermal radiation on magneto nanofluid flow with dusty fluid, *Journal of Applied and Computational Mechanics*, 6(1), 2020, 171-182.
[26] Sheikholeslami, M., Bandpy, M.G., Ellahi, R., Hassan, M. and Soleimani, S., Effects of MHD on Cu–water nanofluid flow and heat transfer by means of CVFEM, *Journal of Magnetism and Magnetic Materials*, 349, 2014, 188-200.
[27] Narender, G., Govardhan, K. and Sreedhar Sarma, G., MHD Casson nanofluid past a stretching sheet with the effects of viscous dissipation, chemical reaction and heat source/sink, *Journal of Applied and Computational Mechanics*, 2019, doi: 10.22055/JACM.2019.14804.
[28] Hashemi-Tilehnoee, M., Dogonchi, A.S., Seyyedi, S.M. and Sharifpur, M., Magneto-fluid dynamic and second law analysis in a hot porous cavity filled by nanofluid and nano-encapsulated phase change material suspension with different layout of cooling channels, *Journal of Energy Storage*, 31, 2020, 101720.
[29] Mondal, S., Dogonchi, A.S., Tripathi, N., Waqas, M., Seyyedi, S.M., Hashemi-Tilehnoee, M. and Ganji, D.D., A theoretical nanofluid analysis exhibiting hydromagnetics characteristics employing CVFEM, *Journal of the Brazilian Society of Mechanical Sciences and Engineering*, 42(1), 2020, 1-12.
[30] Chamkha, A.J., Abbasbandy, S., Rashad, A.M. and Vajravelu, K., Radiation effects on mixed convection about a cone embedded in a porous medium filled with a nanofluid, *Meccanica*, 48(2), 2013, 275-285.
[31] Haroun, N.A., Mondal, S. and Sibanda, P., Hydromagnetic nanofluids flow through a porous medium with thermal radiation, chemical reaction and viscous dissipation using the spectral relaxation method, *International Journal of Computational Methods*, 16(06), 2019, 1840020.
[32] Rashid, M., Khan, M.I., Hayat, T., Khan, M.I. and Alsaedi, A., Entropy generation in flow of ferromagnetic liquid with nonlinear radiation and slip condition, *Journal of Molecular Liquids*, 276, 2019, 441-452.
[33] Pordanjani, A.H., Aghakhani, S., Karimipour, A., Afrand, M. and Goodarzi, M., Investigation of free convection heat transfer and entropy generation of nanofluid flow inside a cavity affected by magnetic field and thermal radiation, *Journal of Thermal Analysis and Calorimetry*, 137(3), 2019, 997-1019.
[34] Mahian, O., Kianifar, A., Sahin, A.Z. and Wongwises, S., Entropy generation during Al_2O_3/water nanofluid flow in a solar collector: Effects of tube roughness, nanoparticle size, and different thermophysical models, *International Journal of Heat and Mass Transfer*, 78, 2014, 64-75
[35] Khan, M.I., Qayyum, S., Hayat, T., Waqas, M., Khan, M.I. and Alsaedi, A., Entropy generation minimization and binary chemical reaction with Arrhenius activation energy in MHD radiative flow of nanomaterial, *Journal of Molecular Liquids*, 259, 2018, 274-283.
[36] Khan, M.W.A., Khan, M.I., Hayat, T. and Alsaedi, A., Entropy generation minimization (EGM) of nanofluid flow by a thin moving needle with nonlinear thermal radiation, *Physica B: Condensed Matter*, 534, 2018, 113-119.
[37] Ibáñez, G., López, A., Pantoja, J. and Moreira, J., Entropy generation analysis of a nanofluid flow in MHD porous microchannel with hydrodynamic slip and thermal radiation, *International Journal of Heat and Mass Transfer*, 100, 2016, 89-97.
[38] Thumma, T., Mishra, S., Bég, O., ADM Solution for Cu-CuO-Water Viscoplastic nanofluid transient slip flow from a porous stretching sheet with entropy generation, convective wall temperature and radiative effects, *Journal of Applied and Computational Mechanics*, 7(3), 2021, 1291-1305.
[39] Shukla, N., Rana, P., Kuharat, S., Anwar Bég, O., Non-similar radiative bioconvection nanofluid flow under oblique magnetic field with entropy generation, *Journal of Applied and Computational Mechanics*, 2021, doi: 10.22055/jacm.2020.33580.2250.
[40] Al-Rashed, A.A., Kolsi, L., Hussein, A.K., Hassen, W., Aichouni, M. and Borjini, M.N., Numerical study of three-dimensional natural convection and entropy generation in a cubical cavity with partially active vertical walls, *Case Studies in Thermal Engineering*, 10, 2017, 100-110.
[41] Hussein, A.K., Lioua, K., Chand, R., Sivasankaran, S., Nikbakhti, R., Li, D., Naceur, B.M. and Habib, B.A., Three-dimensional unsteady natural convection and entropy generation in an inclined cubical trapezoidal cavity with an isothermal bottom wall, *Alexandria Engineering Journal*, 55(2), 2016, 741-755.
[42] Lioua, K., Oztop, H.F., Borjini, M.N. and Al-Salem, K., Second law analysis in a three dimensional lid-driven cavity, *International Communications in Heat and Mass Transfer*, 38(10), 2011, 1376-1383.
[43] Lide, D.R., (Ed.) *CRC Handbook of Chemistry and Physics*, CRC Press, Boca Raton, FL., 1990.

[44] Das, S.K., Putra, N., Thiesen, P. and Roetzel, W., Temperature dependence of thermal conductivity enhancement for nanofluids, *Journal of Heat Transfer*, 125(4), 2003, 567-574.
[45] Saikrishnan, P., Roy, S., Non-uniform slot injection (suction) into water boundary layers over (i) a cylinder and (ii) a sphere, *International Journal of Engineering Science*, 41(12), 2003, 1351-1365.
[46] Das, S.K., Choi, S.U., Yu, W. and Pradeep, T., *Nanofluids: science and technology*, John Wiley & Sons, New Jersey, 2007.
[47] Brinkman, H.C., The viscosity of concentrated suspensions and solutions, *The Journal of Chemical Physics*, 20(4), 1952, 571-571.
[48] Bejan, A., *Convection Heat Transfer*, John Wiley & Sons, New York, 2013.
[49] Ellahi, R., Hassan, M. and Zeeshan, A., Shape effects of nanosize particles in Cu-H_2O nanofluid on entropy generation, *International Journal of Heat and Mass Transfer*, 81, 2015, 449-456.
[50] Arpaci, V.S., Radiative entropy production-lost heat into entropy, *International Journal of Heat and Mass Transfer*, 30(10), 1987, 2115-2123.
[51] Woods, L.C., *Thermodynamics of Fluid Systems*, Oxford Univ. Press, Oxford, 1975.
[52] Bellman, R.E., Kalaba, R.E., *Quasilinearization and Non-Linear Boundary Value Problems*, American Elsevier Publishing Co., New York, 1965.
[53] Varga, R.S., *Matrix Iterative Analysis*, Springer, Berlin, Heidelberg, 2000.
[54] Abu-Nada, E., Masoud, Z., Hijazi, A., Natural convection heat transfer enhancement in horizontal concentric annuli using nanofluids, *International Communications in Heat and Mass Transfer*, 35(5), 2008, 657-665.

Appendix

$$a_1 = \frac{b_2\Delta T}{b_1 + b_2 T_\infty},\;\; a_2 = b_1 + b_2 T_\infty,\;\; a_3 = a_1 a_2,\;\; d_2 = c_1 + c_2 T_\infty,\;\; d_2 = c_2 \Delta T$$

$$P_1 = a_2 k_s + 2C_p d_1 - 2\phi\left(C_p d_1 - a_2 k_s\right),\; P_2 = a_3 k_s + 2C_p d_2 - 2\phi\left(C_p d_2 - a_3 k_s\right),\;\; P_3 = a_2 k_s + 2C_p d_1 + \phi\left(C_p d_1 - a_2 k_s\right),\;\; P_4 = a_3 k_s + 2C_p d_2 + \phi\left(C_p d_2 - a_3 k_s\right)$$

$$N = \frac{1}{1 + a_1 G},\;\; Pr = \frac{1}{d_1 + d_2 G}$$

$$P_5 = \frac{P_1 + P_2 G}{P_3 + P_4 G};\quad P_6 = \frac{d_2 - a_1 d_1}{(1 + a_1 G)^2};\;\; P_7 = \frac{P_2 P_3 - P_1 P_4}{(P_3 + P_4 G)^2};\;\; P_8 = -a_1 \frac{(d_2 - a_1 d_1)}{(1 + a_1 G)^3};\;\; P_9 = -P_4 \frac{(P_2 P_3 - P_1 P_4)}{(P_3 + P_4 G)^3};$$

$$S_1 = \left\{1 - \left(1 - \frac{(\beta\rho)_s}{(\beta\rho)_f}\right)\phi\right\}\sqrt{(1-\phi)^5},\;\; S_2 = \left\{1 - \left(1 - \frac{(\rho)_s}{(\rho)_f}\right)\phi\right\}\sqrt{(1-\phi)^5},\;\; S_3 = \left\{1 - \left(1 - \frac{(C_p\rho)_s}{(C_p\rho)_s}\right)\phi\right\}$$

$$K_1 = \left\{\frac{\sigma_f + 2\sigma_s - 2\phi\left(\sigma_f - \sigma_s\right)}{\sigma_f + 2\sigma_s + \phi\left(\sigma_f - \sigma_s\right)}\right\}\sqrt{(1-\phi)^5}$$

$$A_1 = N,\;\; A_2 = -a_1 G_\eta N^2 + S_2\left[f + \xi f_\xi\left(\frac{1-m}{1+m}\right)\right],\;\; A_3 = -S_2 \xi F\left(\frac{1-m}{1+m}\right),\;\; A_4 = -S_2\left[\frac{4m}{1+m}F + \left(\frac{1-m}{1+m}\right)\xi F_\xi\right] + \xi^2 (Ma)^2 K_1$$

$$A_5 = -a_1 F_\eta N^2,\;\; A_6 = -a_1 F_{\eta\eta} N^2 + 2a_1^2 F_\eta G_\eta N^3 + S_1 \frac{2\lambda}{1+m}\;\; A_7 = -S_2\left[\frac{2m}{1+m}\left(1 + F^2\right) + \left(\frac{1-m}{1+m}\right)\xi F F_\xi\right] - a_1 F_\eta G_\eta N^2 - a_1 F_{\eta\eta} G N^2 + 2a_1^2 F_\eta G_\eta G N^3$$

$$M_1 = \frac{N}{Pr}[P_5 + R],\;\; M_2 = 2G_\eta\left[P_5 P_6 + \frac{N}{Pr}P_7\right] + \frac{S_3}{1+m}\left((1+m)f + (1-m)\xi f_\xi\right),\;\; M_3 = -S_3 \xi F\left(\frac{1-m}{1+m}\right)$$

$$M_4 = G_{\eta\eta}\left[P_6\left(P_5 + R\right) + \frac{N}{Pr}P_7\right] + 2G_\eta^2\left[P_6 P_7 + P_5 P_8 + \frac{N}{Pr}P_9\right],\;\; M_5 = -S_3 \xi G_\xi\left(\frac{1-m}{1+m}\right)$$

$$M_6 = G_\eta^2\left[P_5 P_6 + \frac{N}{Pr}P_7\right] + G G_\eta\left[\left(P_5 + R\right)P_6 + \frac{N}{Pr}P_7\right] + 2G G_\eta^2\left[P_6 P_7 + P_5 P_8 + \frac{N}{Pr}P_9\right] - S_3 \xi F G_\xi\left(\frac{1-m}{1+m}\right)$$

ORCID iD

Tapas Barman https://orcid.org/0000-0001-9733-9163
S. Roy https://orcid.org/0000-0002-7083-0822
Ali J. Chamkha https://orcid.org/0000-0002-8335-3121

How to cite this article: Barman T., Roy S., Chamkha A.J. Magnetized Bi-convective Nanofluid Flow and Entropy Production Using Temperature-Sensitive Base Fluid Properties: A Unique Approach, *J. Appl. Comput. Mech.*, 8(4), 2022, 1163–1175. https://doi.org/10.22055/JACM.2021.38204.3177